

Data-educed broadband equivalent acoustic source model for supersonic jet noise

Tracianne B. Neilsen, Aaron B. Vaughn, Kent L. Gee, Masahito Akamine, Koji Okamoto, Susumu Teramoto, and Seiji Tsutsumi

Citation: *The Journal of the Acoustical Society of America* **146**, 3409 (2019); doi: 10.1121/1.5132947

View online: <https://doi.org/10.1121/1.5132947>

View Table of Contents: <https://asa.scitation.org/toc/jas/146/5>

Published by the [Acoustical Society of America](#)

ARTICLES YOU MAY BE INTERESTED IN

[Acoustic wave propagation in effective graded fully anisotropic fluid layers](#)

The Journal of the Acoustical Society of America **146**, 3400 (2019); <https://doi.org/10.1121/1.5131653>

[Three-dimensional reflector localisation and room geometry estimation using a spherical microphone array](#)

The Journal of the Acoustical Society of America **146**, 3339 (2019); <https://doi.org/10.1121/1.5130569>

[Sensitivity analysis of a parabolic equation model to ground impedance and surface roughness for wind turbine noise](#)

The Journal of the Acoustical Society of America **146**, 3222 (2019); <https://doi.org/10.1121/1.5131652>

[A tutorial example of duct acoustics mode detections with machine-learning-based compressive sensing](#)

The Journal of the Acoustical Society of America **146**, EL342 (2019); <https://doi.org/10.1121/1.5128399>

[Calculation of acoustic radiation modes by using spherical waves and generalized singular value decomposition](#)

The Journal of the Acoustical Society of America **146**, EL347 (2019); <https://doi.org/10.1121/1.5128139>

[Compensating for source directivity in immersive wave experimentation](#)

The Journal of the Acoustical Society of America **146**, 3141 (2019); <https://doi.org/10.1121/1.5131029>



The banner features a background image of a 3D printer nozzle printing a red, lattice-structured part. On the left, the JASA logo is displayed in white, with the text 'THE JOURNAL OF THE ACOUSTICAL SOCIETY OF AMERICA' underneath. To the right of the logo, the text 'Special Issue: Additive Manufacturing and Acoustics' is written in yellow and white. At the bottom left, a yellow button contains the text 'Submit Today!'.

Data-educed broadband equivalent acoustic source model for supersonic jet noise

Tracianne B. Neilsen,^{a)} Aaron B. Vaughn, and Kent L. Gee
Department of Physics and Astronomy, Brigham Young University, Provo, Utah 84602, USA

Masahito Akamine and Koji Okamoto
University of Tokyo, Kashiwa, Chiba, 277-8561, Japan

Susumu Teramoto
University of Tokyo, Bunkyo-ku, Tokyo, 113-8656, Japan

Seiji Tsutsumi
Japan Aerospace Exploration Agency, Sagamihara, Kanagawa, 252-5210, Japan

(Received 19 April 2019; revised 17 September 2019; accepted 18 October 2019; published online 19 November 2019)

A broadband equivalent acoustic source distribution can be used to model the sound field near a high-speed jet. Such models must account for the spatio-spectral variation of the sound levels. This work presents a technique for obtaining such a model using a spectral decomposition method associated with large and fine-scale turbulent mixing noise to create broadband equivalent source distributions for each noise type. The large-scale turbulent mixing noise is represented by frequency-dependent wavepackets, while the fine-scale turbulent mixing noise is modeled as a frequency-dependent incoherent, extended source distribution. This technique is applied to acoustical measurements from an ideally expanded, unheated Mach 1.8 jet. The wavepackets model the sound field levels in the maximum radiation region, but the second incoherent source distribution is required to obtain the levels at the other locations. The combination of the incoherent source distribution and the wavepacket provides a broadband, equivalent acoustic source representation that adequately models the sound field for Strouhal numbers between 0.04 and 0.25. At higher Strouhal numbers, better agreement is obtained when accounting for a frequency-dependent shift in the apparent acoustic source region. This frequency-dependent source region is more important closer to the jet than in the far field. © 2019 Acoustical Society of America.

<https://doi.org/10.1121/1.5132947>

[AL]

Pages: 3409–3424

I. INTRODUCTION

The impact of noise from supersonic jet flow from high-performance military aircraft often needs to be predicted to establish auditory risk for personnel, e.g., flight crew personnel working on an aircraft carrier deck, and annoyance for communities. Because precise computational modeling of the turbulent flow and associated sound radiation for military aircraft engines has not yet been achieved, a reduced-order source model is sought from acoustical measurements. A broadband, data-educed equivalent acoustic source model (ESM) for sound levels near the jet can be obtained by the process described in this paper. This ESM contains information about the frequency and spatial variation of the noise sources. Noise measured near a laboratory-scale, Mach 1.8 jet^{1,2} establishes this methodology as a precursor to applying the method to military aircraft noise.

An ESM is a data-based source characterization method³ that uses some *a priori* knowledge of, or assumption regarding, the source characteristics.^{4,5} Lighthill's⁶ famous acoustic analogy is often called an ESM. McLaughlin *et al.*⁷ developed an uncorrelated, symmetric ESM in examining the impact of a

ground reflecting plane on supersonic laboratory-scale jet noise. ESMs have also been obtained using phased-array methods, such as near-field acoustical holography applied to laboratory-scale jet noise^{8,9} and noise from high-performance military aircraft.^{10,11} Beamforming has also been applied to noise from laboratory-scale jets (cf. Refs. 12–15) and high-performance military aircraft.¹⁶ For this same aircraft, a simple ESM was obtained empirically at a few discrete frequencies by Morgan *et al.*¹⁷

The current ESM uses two extended source distributions, similar to Ref. 17, but the distributions are directly inferred, or educed, from the data. This broadband data-education technique is based on decomposing measured spectral densities into the fine scale similarity (FSS) and large-scale similarity (LSS) spectra proposed by Tam *et al.* and Tam and Zaman^{18,19} The similarity spectra have been interpreted as representing the noise from two types of turbulent mixing noise. Many studies have observed the difference between the sideline noise attributed to fine-scale turbulent structures and the louder, directional radiation attributed to the large-scale turbulent structures.^{20–23} One candidate ESM for large-scale turbulent structures is a wavepacket.

One method for obtaining a wavepacket ESM uses an LSS spectral decomposition to obtain frequency-dependent,

^{a)}Electronic mail: tbn@byu.edu

axial wavenumber spectra (spatial Fourier transforms of axial wavepackets). Morris applied this method to far-field spectra from laboratory-scale jets operating at different jet velocities.²⁴ This method was combined with an analytical wavepacket model in Neilsen *et al.*²⁵ to obtain a wavepacket ESM of the directional component of noise from a high-performance military aircraft.

The wavepacket ESM can be used to model sound field levels. However, the resulting wavepacket ESM captures only the directional radiation and underestimates levels at other locations. Thus, a second source distribution must be added to the ESM. In prior work by Papamoschou,^{26,27} a monopole was added to a wavepacket ESM to increase levels outside the maximum radiation direction. A different approach is taken in this paper: The FSS spectral decomposition is used to obtain an extended source distribution.

This ESM technique and its potential for sound field modeling are explored in this paper. First, this ESM technique highlights the importance of carefully choosing the origin used to define angles for analyses and modeling close to the jet. (“Close to the jet” in this paper means outside the hydrodynamic near field but in the geometric near field.) While a constant origin suffices at low frequencies, higher frequencies require a frequency-dependent origin. Second, this ESM technique shows the advantage of adding an extended, incoherent source distribution to the wavepacket ESM. This addition models the levels outside the maximum radiation region. Third, this ESM can use inputs at one location to learn about the equivalent acoustic source, such as estimating the convective velocity, and to predict sound levels at other locations.

To demonstrate these points prior to application to military aircraft noise, a data-duced, broadband ESM is developed for supersonic, laboratory-scale jet noise. Background about prior wavepacket modeling is provided in Sec. II. The methods for the current ESM are presented in Sec. III. These methods are applied to noise from an unheated, Mach 1.8 jet,^{1,2} as explained in Sec. IV. Results of applying this ESM technique, modeling sound field levels, and estimating convective speed are given in Sec. V. The results demonstrate the benefit of combining an LSS-based wavepacket with an FSS-based extended source distribution in modeling sound levels and highlight the need for a frequency-dependent definition of an apparent maximum source region to improve sound field modeling close to the jet.

II. BACKGROUND

Wavepackets are commonly used in optics, quantum mechanics, and acoustics when a localized wave travels as a unit. The idea that the directive portion of jet noise²⁸ can be modeled by a wavepacket was formalized by Crighton and Huerre.²⁹ Since then, the wavepackets ansatz has been used for modeling jet turbulence; work prior to 2013 is reviewed in Ref. 30. More recently, linear stability analyses on LES simulations (cf. Refs. 31 and 32) have obtained wavepacket representations. Other recent work has focused on the effect of forcing function on the optimal resonance^{33,34} (usually representing an azimuthally symmetric wavepacket) and on

higher-order³⁵ and higher-frequency³⁶ wavepackets. Jeun *et al.*³⁷ conducted an input-output analysis for supersonic jets found that the optimal mode resembles a wavepacket and dominates the response but that additional sub-optimal modes also contribute, which are not captured by a single wavepacket model.

Several studies have shown the connection between wavepacket models and the directional³⁸ partially correlated³⁹ jet noise field.⁴⁰ Cavalieri and Agarwal⁴¹ found significant correlation between sound at low angles and axisymmetric wavepacket structures in the jet. Reba *et al.*⁴² used two-point, space-time correlations to extract wavepackets from hydrodynamic pressure fluctuations, Sinha *et al.*⁴³ used parabolized stability equations to model an average wavepacket, and Maia *et al.*⁴⁴ used particle-image velocimetry measurements to extract wavepacket parameters. In Refs. 42–44, the wavepackets could predict sound levels over a narrow angular aperture for small polar angles (relative to the jet axis). These flow-based or near-field wavepackets are, however, fundamentally different than wavepacket models derived from the radiated sound.

In this work, the frequency-dependent wavepackets are deduced from the spectral densities associated with the directional component of jet noise. The equivalent acoustic wavepackets model a source distribution projected on a near-field cylinder centered on the jet axis. Papamoschou^{26,27} proposed an analytical wavepacket models that can be optimized to fit the far-field sound levels in the maximum sound radiation region. A similar approach was taken by Baars and Tinney⁴⁵ to generate both near and far-field acoustic signatures. Koenig *et al.*⁴⁶ used an orthogonal decomposition of acoustical far-field measurements of a subsonic, cold laboratory jet and compared a single modal component to a wavepacket model. Du and Morris⁴⁷ applied conventional beamforming to simulated far-field jet noise data to obtain the acoustic complex pressure at the jet lip-line, which was then decomposed using a wavepacket model for Strouhal numbers, St , of 0.3 and 0.6. When compared to the simulated far-field pressure measurements, the estimated pressure field from the first wavepacket mode showed general agreement. Reba *et al.*⁴² measured the hydrodynamic pressure field and fit the amplitude and correlation measurements to Gaussian-shaped wavepackets of the first two azimuthal modes, a method also used by Schlinker *et al.*^{48,49} Morris²⁴ showed how the spatial distribution of levels from the LSS spectral decomposition yield frequency-dependent, axial wavenumber for data-duced wavepackets. This approach was applied to a wavepacket-based ESM of the directional component of noise from a high-performance military aircraft.²⁵

Due to the latitude in performing the spectral decompositions, the resulting ESM likely becomes a surrogate of the azimuthal-mode decomposition from experimental and computation modeling of the turbulent flow. In these models, often the axisymmetric mode only dominates radiation at lower angles (relative to the jet centerline) and lower St ,⁴¹ whereas radiation at larger angles and St that are dominated by higher-order, helical modes.³¹ One way to connect wavepackets to these azimuthal decompositions is to consider the LSS-based wavepacket as a proxy for the azimuthal mode,

and the FSS-based source distribution as representing the contributions of the helical modes. In terms of the input-output analysis by Jeun *et al.*,³⁷ the LSS-based wavepacket is analogous to the optimal mode and the FSS-based distribution to the coherent mechanism associated with suboptimal modes.

III. METHODS

In this paper, two methodologies are linked together and expanded to create a frequency-dependent ESM for noise near an ideally expanded, Mach 1.8 laboratory-scale jet. The theoretical foundations for similarity spectral decomposition, reduction of the wavenumber spectra, examples of LSS-based wavepackets, estimates of the convective speed, and sound field modeling are presented in this section.

A. Similarity spectra decompositions

From an extensive database of far-field, laboratory-scale, ideally expanded jet data, Tam *et al.* and Tam and Zaman^{18,19} found empirical similarity spectra for each type of turbulent mixing noise. The LSS spectrum, which has a relatively narrow peak and power-law decay on both sides, approximates the spectrum of the high-amplitude, directional radiation associated with large-scale turbulent structures.^{4,22,24,42,49} On the other hand, the FSS spectrum—with its broader peak and a more gradual roll-off at both high and low frequencies—matches the radiated spectra in the sideline and forward directions. In between these two regions, a combination of the FSS and LSS spectra is needed to account for the spectral shape. Although there is latitude in performing the decomposition, many examples show good agreement with measured jet noise spectra: See Refs. 4, 21, 22, 24, 48, and 50–52 for applications to laboratory-scale jet noise, Ref. 53 for CFD simulations of jet noise, and Refs. 5, 23, and 54 for military aircraft engine noise.

The similarity spectra were developed from far-field measurements, so questions arise as to their applicability close to the jet. The closest distance at which the similarity spectra have previously been compared to measured spectra was at approximately $18D$ from the shear layer on a 30 m long array placed near a high-performance military aircraft.²³ The current work investigates the applicability even closer for laboratory-scale jets, at just $10D$ from the jet centerline in Sec. V A and finds a consistent interpretation as long as care is taken in defining the angular regions.

B. Wavepacket ESM

A collection of wavepackets—one for each frequency, ω —comprises a broadband ESM distribution on a cylinder extending from the nozzle lip line in the $+z$ direction. The spatial Fourier transform of each wavepacket is an axial wavenumber spectrum, $G(k_z, \omega)$. The magnitude of $G_0(k_z, \omega)$ can be estimated from the $S(\mathbf{r}_1, \omega)$, following the derivation in Ref. 24.

For this work, azimuthal symmetry is assumed, which is often a good approximation, especially for lower frequency noise from axisymmetric jets.^{14,24} Analyses have shown that

only modes with low azimuthal order contribute significantly in the far field in the maximum radiation region.^{26,44} The assumption of azimuthal symmetry is also applicable if the measurements span a limited azimuthal aperture so as to lack sufficient information to estimate the contributions from higher-order azimuthal modes ($n > 0$).⁵⁵ In this case, an azimuthally averaged result is obtained and labeled $G_0(k_z, \omega)$.

The derivation of the LSS-based wavenumber spectrum culminates in Eq. (24) of Ref. 24. The relationship between $S(\mathbf{r}_1, \omega)$ and $G_0(k_z, \omega)$ is

$$\frac{A^2 |G_0(k_z, \omega)|^2}{D^2} = \frac{\pi}{2\rho_j^2 U_j^3} \left(\frac{R_1}{D}\right)^2 |H_0^{(1)}(k_r r_0)|^2 \frac{S(\mathbf{r}_1, \omega)}{D}, \quad (1)$$

where D and r_0 are the diameter and radius of the jet nozzle, ρ_j and U_j are the density and speed of the jet, and A is a normalization factor. $H_0^{(1)}$ is the zeroth-order Hankel function of the first kind, and k_r is the radial wavenumber. The square-root of the left-hand side of Eq. (1) is referred to hereafter as $|G_0(k_z)|$. Examples of $S(\mathbf{r}_1, \omega)$ and $|G_0(k_z)|$ for the Mach 1.8 jet are shown in Sec. V B.

1. Educed wavenumber spectra

The estimate of $|G_0(k_z)|$ depends on the values of k_z , which are based on the definition of θ , the polar angle relative to the jet centerline. In cylindrical coordinates, the angle at which the wavenumber vector, \mathbf{k} , points relative to the z axis is $\theta = \tan^{-1}(k_r/k_z)$. The wavenumber associated with radial direction, $k_r = \pm\sqrt{k^2 - k_z^2}$ is real if $k_z \leq k$ and, in such cases, corresponds with waves propagating away from the source. Such wavenumbers are called sonic (when $k_z = k$) or supersonic (when $k_z < k$), signifying trace wavenumber matching in the axial direction. For the subsonic wavenumbers ($k_z > k$), k_r is imaginary. Only wavenumbers with $k_z \leq k$ (corresponding to real values of θ) are used in calculating $|G_0(k_z)|$ because $S(\mathbf{r}_1, \omega)$ comes from the propagating acoustic field and, thus, does not contain information about the evanescent components.

2. Equivalent acoustic wavepackets

The equivalent acoustic wavepackets are the inverse Fourier transform of the educed wavenumber spectra. However, because $|G_0(k_z)|$ can be educed only for supersonic k_z , an optimization procedure is required to estimate the wavepackets. Each frequency-dependent wavepacket represents a pressure fluctuation on a cylindrical surface concentric with the jet nozzle of radius $r_0 = D/2$, which can be expressed as

$$p_w(z, t) = p_0(z) e^{-i\omega t}, \quad (2)$$

where t is time, and z is the distance downstream from the jet nozzle exit plane. The wavepacket axial shape, $p_0(z)$, is typically composed of an amplification-decay envelope and an oscillating portion: $p_0(z) = |p_0(z)| e^{i\alpha z}$, where $\alpha = \omega/U_c$ is the wavenumber associated with the peak in the wavenumber spectrum.^{26,27,42}

Although many options exist for $|p_0(z)|$, an asymmetric Gaussian model is implemented, as was used in Ref. 46. The candidate wavepacket model at frequency ω is

$$p_0(z) = \epsilon(\omega)B(z)e^{i\alpha z}. \quad (3)$$

$B(z)$ is a piecewise continuous, asymmetric Gaussian distribution

$$B(z) = \begin{cases} e^{-b_1(z-z_0)}, & \text{for } z \leq z_0 \\ e^{-b_2(z-z_0)}, & \text{for } z > z_0, \end{cases} \quad (4)$$

where z_0 is the location of the peak of the distribution, and b_1 and b_2 represent the rate of growth and decay of the axial amplitude distribution, respectively.

Estimates of frequency-dependent wavepackets are obtained by a simulated annealing optimization. The optimization finds the set of modeling parameters $\mathbf{m} = [\alpha, b_1, b_2, \epsilon]$ that minimizes the difference between the magnitude of the spatial Fourier transform of $p_0(z)$ ($\hat{P}_0(k_z) = \mathcal{F}\{p_0(z)\}$) and $|G_0(k_z)|$ from Eq. (1). Specifically, the wavepacket modeling parameters, \mathbf{m} , are found that minimize the cost function, E ,

$$E(\mathbf{m}) = \sum_{i=1}^N \left[\frac{|\hat{P}_0(k_{z,i}, \mathbf{m})|}{\hat{P}_{0,\max}(\mathbf{m})} - \frac{|G_0(k_{z,i})|}{G_{0,\max}} \right]^2,$$

where $\hat{P}_{0,\max}(\mathbf{m})$ and $G_{0,\max}$ are the maximum values of the analytical and data-educed wavenumber spectra, respectively, and N is the number of k_z values at which they are compared. In practice, $\hat{P}_0(k_{z,i}, \mathbf{m})$ and $|G_0(k_{z,i})|$ are defined at different k_z values, so an interpolation is necessary before calculating $E(\mathbf{m})$. Estimates of z_0 cannot be obtained using only the magnitudes of the axial wavenumber spectra as a translation of $p_0(z)$ in z correspond to a phase shift in $\hat{P}_0(k_z)$. Examples of wavepackets for the Mach 1.8 jet are given in Sec. VC.

3. Convective velocity

In addition to providing sound field models, the LSS-based wavenumber spectra yield estimates of the convective velocity, U_c . For convectively supersonic, large-scale turbulent structures at frequencies where the educed $|G_0(k_z)|$ has a peak, the wavenumber associated with the peak, $k_{z,\text{peak}}$, provides estimates of U_c and θ_{peak} . The relationship $U_c = \omega/k_{z,\text{peak}}$ provides the phase speed of the axial wavepackets, which are related to the directivity, θ_{peak} : $\cos \theta_{\text{peak}} = k_{z,\text{peak}}/k$. Examples of convective velocities are provided for the Mach 1.8 jet in Sec. VF.

C. Sound level modeling

Both Morris²⁴ and Papamoschou²⁶ describe how the axial wavenumber spectrum of a wavepacket, $G_0(k_z, \omega)$, can be used to model far-field sound pressure levels. For a single angular frequency, ω , the contributions can be divided into two parts corresponding with subsonic and supersonic wavenumbers, as shown in Eq. (3) in Ref. 26, with the supersonic wavenumber contributing to the radiated field. For the case of azimuthal symmetry, the resulting modeled, far-field spectral density for the wavepacket is

$$S_w(\mathbf{r}, \omega) = \left(\frac{\epsilon}{\pi R} \right)^2 \left| \frac{G_0(k_z)}{H_0^{(1)}(k_r r_0)} \right|^2, \quad (5)$$

where ϵ is a frequency-dependent scaling factor. [“Far field” in this derivation means that the asymptotic form of $|H_0^{(1)}(k_r r_0)|$ can be used. For the 10D locations in this study, the asymptotic form is a reasonable numerical approximation for $\text{St} > 0.04$.]

The modeled field in Eq. (5) can be used with the $|G_0(k_z)|$ for any selected wavepacket distribution. When the $|G_0(k_z)|$ educed from the similarity spectra decomposition in Eq. (1) is employed in Eq. (5), the resulting expression for the wavepacket generated field at \mathbf{r}_2 reduces to a spherical spreading for the portion of the field at \mathbf{r}_1 assigned to the LSS spectrum: $S_w(\mathbf{r}_2) = (R_1/R_2)S_w(\mathbf{r}_1)$. However, the difficult part of applying spherical spreading to jet noise is identifying the directions the sound is traveling, especially when different noise components originate at different regions. When modeling the field from an ESM with multiple source distributions, Eq. (5) yields the portions of the field generated by the different distributions, as is shown in Sec. VD.

The associated sound levels, in decibels, modeled at the location \mathbf{r}_2 are

$$L_w(\mathbf{r}_2, \omega) = 10 \log \left(\frac{S_w(\mathbf{r}_2, \omega)}{p_{\text{ref}}^2} \right), \quad (6)$$

where $p_{\text{ref}} = 20 \mu\text{Pa}/\sqrt{\text{Hz}}$. These modeled levels can be compared to measured levels to evaluate the validity of this level-based, broadband, wavepacket model for the large-scale turbulent mixing noise, as shown in Sec. VD.

D. Extended, incoherent ESM

The far-field levels generated from a single wavepacket, as in Eq. (6), do not adequately model the spatial radiation pattern of jet noise at a single frequency.^{26,47} The modeled L_w captures the directional radiation but not the sound levels outside of the maximum radiation region. To match the jet noise sound levels to the sideline of the nozzle exit (large polar angles), Papamoschou²⁶ added a monopole to his wavepacket model. A different approach is taken in this paper: A second incoherent, extended source distribution is included to account for the sideline levels. This second distribution is obtained from the spatially varying FSS spectral decomposition using Eq. (1) and yields modeled spectral densities, $S_i(\mathbf{r}, \omega)$, similar to Eq. (5).

The total modeled sound field is a combination of the sound from the LSS-based wavepacket, $S_w(\mathbf{r}, \omega)$, and the FSS-based incoherent distribution, $S_i(\mathbf{r}, \omega)$. The total modeled spectral levels are

$$L_{\text{tot}}(\mathbf{r}, \omega) = 10 \log \left(\frac{S_w(\mathbf{r}, \omega) + S_i(\mathbf{r}, \omega)}{p_{\text{ref}}^2} \right). \quad (7)$$

Because S_w and S_i are based on the spectral decomposition, the resulting L_{tot} does not include artifacts in the measurements,

such as from scattering and reflections. Thus, L_{tot} gives an idealized model of the field solely from the noise that was ascribed to the similarity spectra. The ability of the ESM to obtain measured spectral levels is evaluated in Sec. VD.

IV. MEASUREMENTS

This sound field modeling technique is applied to acoustical measurements from an ideally expanded, Mach 1.8 jet at the Hypersonic High-enthalpy Wind Tunnel at Kashiwa Campus of the University of Tokyo.^{1,2} The unheated jet was ideally expanded through a 20-mm diameter (D), converging-diverging nozzle. Although the facility is not anechoic, nearby reflecting surfaces were wrapped in fiberglass to limit reflections. Favorable matches to anechoic measurements by Greska⁵⁶ were shown previously by Akamine *et al.*¹

Acoustical measurements were made on an arc and a line array, as shown in Fig. 1. The measurement array reference point (MARP), marked as a circle in Fig. 1 at $z = 10D$, represents the origin from which the angles and distances are defined and corresponds to an estimated source location for many frequencies of interest, as confirmed from acoustics intensity vectors in Ref. 57. (While most far-field studies use the nozzle exit plane as the origin, this definition does not work for locations close to the jet, as is discussed in Sec. VA.) The stationary polar microphone arc contained 16 G.R.A.S. 40BE, type 1, prepolarized microphones, which spanned $\theta = 15^\circ$ – 90° , relative to the jet exhaust centerline, with 5° resolution. The line array, $10D$ from and parallel to the jet centerline, consisted of 16 G.R.A.S. 46BG, type 1, prepolarized microphones with sensitivities less than 0.3 mV/Pa, permitting peak sound pressure level measurements above 180 dB. The line array microphones were spaced $1D$ apart. For all measurements, the microphone gridcaps were removed. Additional information about the measurements is found in Ref. 2. Power spectral densities from the $40D$ arc are shown in Fig. 2 of Ref. 57.

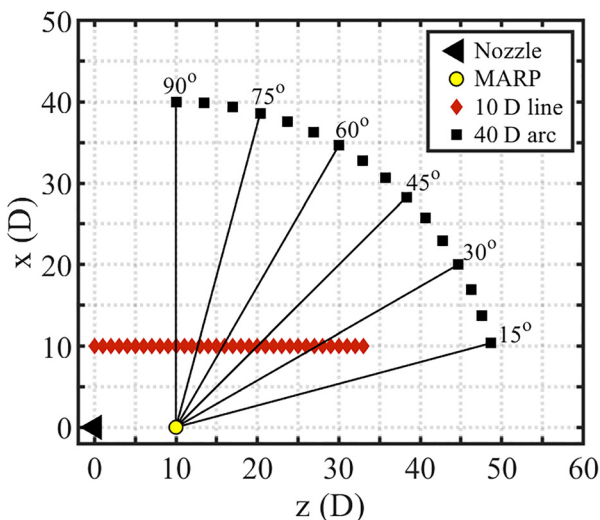


FIG. 1. (Color online) Schematic of the experiment with angles relative to the MARP at $z = 10D$.

V. RESULTS

Each step of the equivalent source model development and resulting sound field modeling is presented for a Mach 1.8, unheated, ideally expanded jet. Examples of how well the similarity spectra match the measured spectral densities are presented in Sec. VA. Educated, LSS-based, axial wavenumber spectra are shown in Sec. VB followed by corresponding wavepackets. The ability of the ESM—consisting of the LSS-based $|G_0(k_z)|$ and the accompanying FSS-based incoherent source distributions—to model measured spectral densities is explored in Sec. VC. A preliminary attempt at including a frequency-dependent MARP is presented in Sec. VD. The difference in estimates of the frequency-dependent, convective velocity between the constant and frequency-dependent MARP cases is shown in Sec. VE.

A. Similarity spectra decompositions

The first step is to decompose the measured spectral densities into portions corresponding with the large- and fine-scale turbulent mixing noise using the empirical similarity spectra defined by Tam *et al.* and Tam and Zaman^{18,19} Details of the similarity spectra decompositions for the Mach 1.8 jet described in Sec. IV are reported in Ref. 52 and summarized here. Examples of similarity spectra fits to the power spectral density (PSD) at select microphones on the $10D$ line array are shown in Fig. 2. The spectral decompositions for the $40D$ arc are shown in Fig. 6 of Ref. [52]. The similarity spectra decompositions match the measured spectral densities and follow the expected spatial trends of FSS spectrum for large θ , LSS spectral shape at small θ , and a combination in between. The agreement at the $10D$ line array indicates that the similarity spectra developed using far-field measurements¹⁸ represent the spatio-spectral variation close to the jet.

Comparisons of the angular regions over which the LSS, FSS, and combined spectra match L_{meas} at the different measurement arrays can potentially yield insights into complex sound propagation paths. To illustrate this point, the spatial regions over which the LSS or FSS spectra, or a combination of the two spectra provide the best fits, are shown in Fig. 3: Each microphone location is coded according to the type of similarity spectra fit (LSS, FSS, or mix). A consistent identification of spectral type is exhibited along radials for the MARP at $z = 10D$, as shown in Fig. 3(a).

To examine whether this choice of the MARP at $10D$ dictates the constancy of similarity spectral decomposition along radials, comparisons are made with other choices for the MARP. For $z = 0$ [in Fig. 3(b)], the propagation radials are no longer consistent. The 36° radial, for example, starts in an FSS region at the $10D$ line array but progresses to a combination region at the arc. The MARP at $z = 15D$ [Fig. 3(c)] also yields inconsistencies on the 56° and 67° radials. Thus, the choice of $z = 10D$ for the MARP provides consistency for the similarity spectra decompositions for this unheated, ideally expanded Mach 1.8 jet, which is important for both the ESM technique and subsequent field modeling.

While similarity spectral decompositions are usually compared to the spectral levels at a single location (as in Fig. 2), the wavenumber spectrum eduction procedure

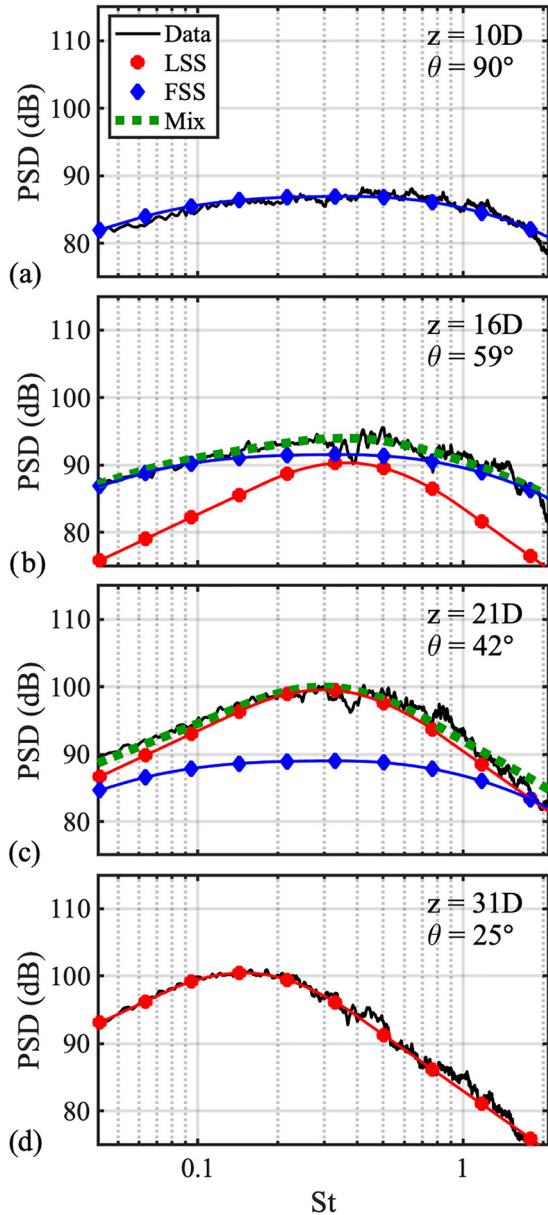


FIG. 2. (Color online) Similarity spectra decompositions of measured spectral density (dB re $20 \mu \text{Pa}/\sqrt{\text{Hz}}$) on the $10D$ line array: measured (unmarked lines), LSS similarity spectrum (circles), FSS similarity spectrum (diamonds), LSS + FSS combined spectrum (dashed).

described in Sec. III A relies on $S(\mathbf{r}_1, \omega)$. Comparisons of the spatial variation is shown in part (a) of Figs. 4–6 for $St = 0.1, 0.2,$ and 0.4 , which correspond to approximately 2.4, 4.8, and 9.6 kHz. An extrapolation is performed to taper the $S(\mathbf{r}_1, \omega)$ to zero at smaller values of z before they are used in Eq. (1) to obtain $|G_0(k_z)|$.

B. Level-educed wavenumber spectra

From the $10D$ line array and the $40D$ arc, two sets of $|G_0(k_z)|$ are obtained using Eq. (1). Examples of $|G_0(k_z)|$ for the $St = 0.1, 0.2,$ and 0.4 are shown in part (b) of Figs. 4–6, as function of $k_z D$ to facilitate comparisons with the cases shown in Ref. 24. Values for $|G_0(k_z)|$ are obtained only for the supersonic, propagating components ($k_z \leq \omega/c$), which correspond to real values of k_r (see Sec. III B 1).

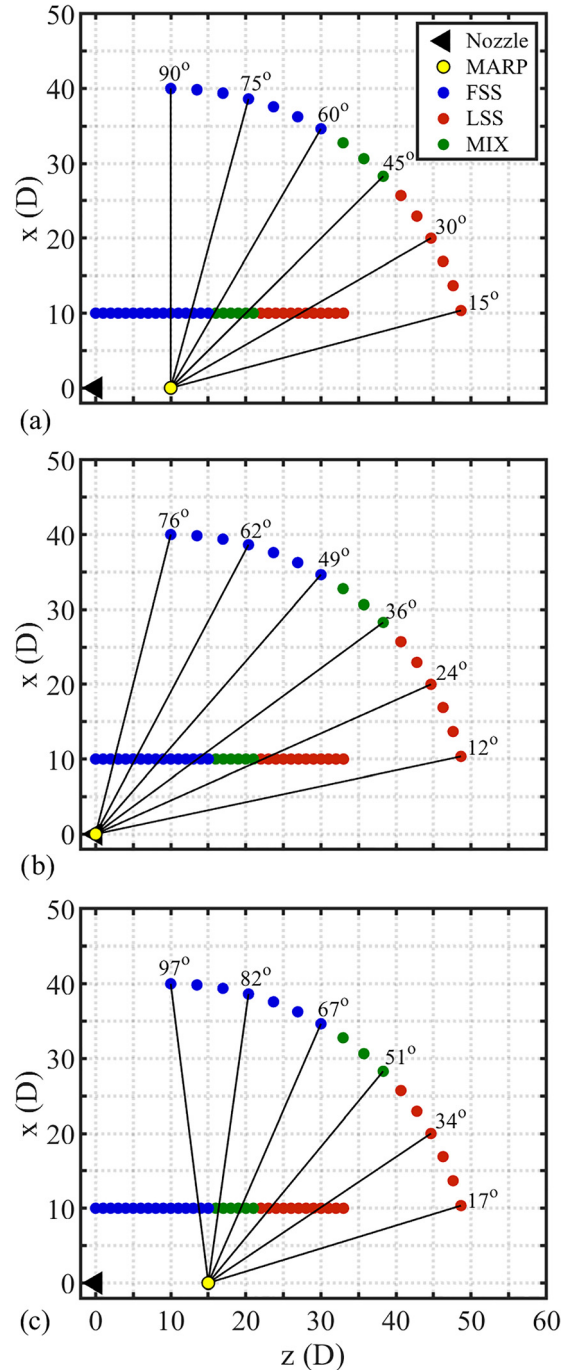


FIG. 3. (Color online) Microphone locations (circles) color-coded based on the type of similarity spectra decomposition that provides the best match. The lines show radials from different MARP locations: (a) $z = 10D$, (b) $z = 0$, and (c) $z = 15D$.

Frequency-dependent variations of $|G_0(k_z)|$, shown in Fig. 7(a) for the $10D$ line array, are similar to those for the far-field examples in in Fig. 4 of Ref. 24. At low St , $|G_0(k_z)|$ increases over the entire range of supersonic k_z values—as seen at $St = 0.1$ for both locations. The lack of a wavenumber peak in $|G_0(k_z)|$ indicates that the jet conditions do not permit trace wavenumber matching, and consequently, indicates a convectively subsonic phase speed at these frequencies. For higher St , the peak in the wavenumber spectra occurs at supersonic k_z . From Fig. 7(a), it appears that more

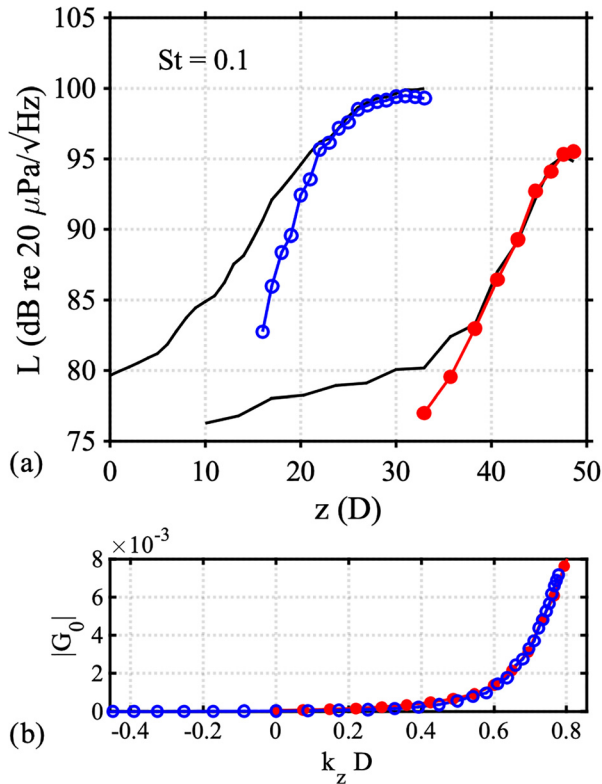


FIG. 4. (Color online) (a) Spectral density levels from measurements (unmarked line) and LSS-based $S(r_1, \omega)$ on the 10D line array (empty circles) and 40D arc (filled circles) at $St = 0.1$, and (b) the corresponding LSS-based axial wavenumber spectra, $|G_0(k_z)|$.

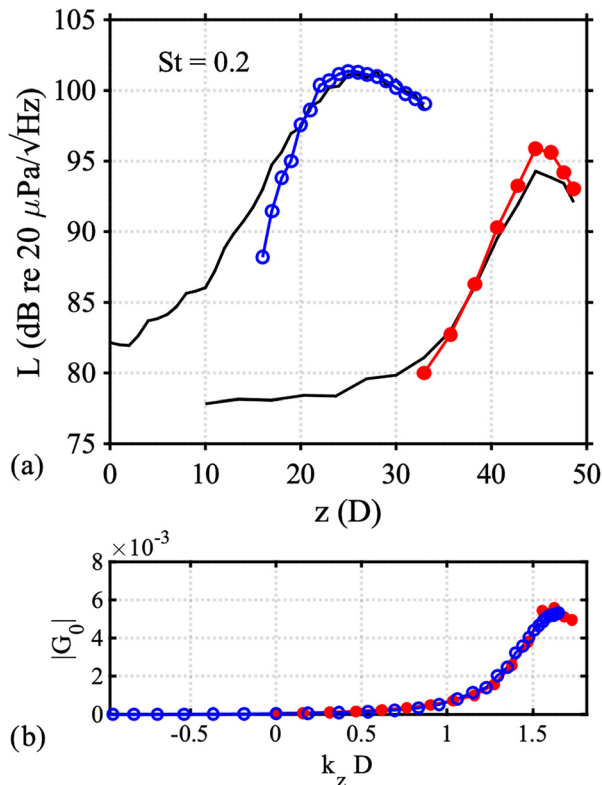


FIG. 5. (Color online) Similar to Fig. 4 but at $St = 0.2$.

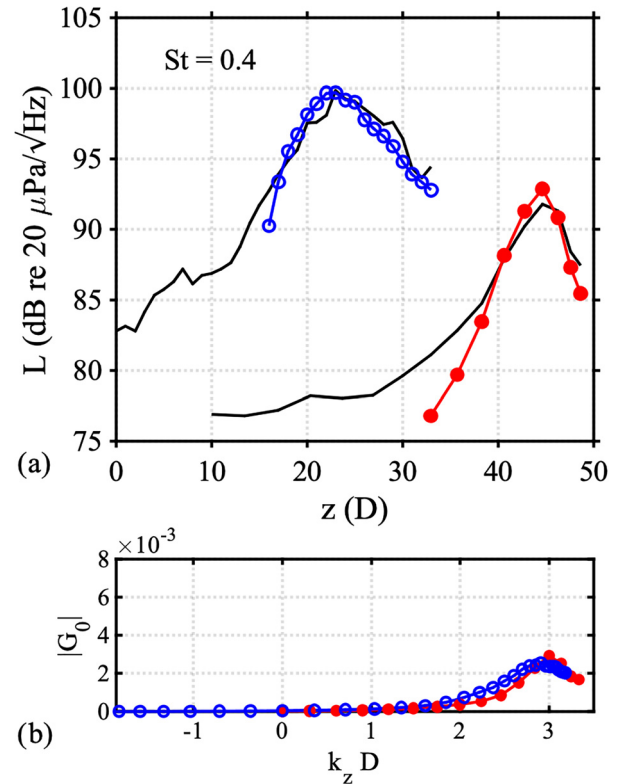


FIG. 6. (Color online) Similar to Fig. 4 but with $St = 0.4$.

of the wavenumber spectrum is convectively supersonic as frequency increases, for octave bands $St = 0.1$ – 1.6 .

These observations, however, need to be reconsidered because of the frequency scaling inherent in the definitions of U_c and θ_{peak} . The impact of this scaling is uncovered by normalizing $|G_0(k_z/k)|$ at each frequency, as shown in Fig. 7(b) at select St for the 10D array. For $St = 0.05$ and 0.1 , the normalized $|G_0(k_z/k)|$ have the same shape and no evidence of a peak indicating convectively subsonic phase speeds across the wavepacket. As St increases, the normalized $|G_0(k_z/k)|$ broaden and a peak appears, signifying convectively supersonic phase speeds. At higher St , the normalized $|G_0(k_z/k)|$ reach a consistent shape and peak value. Uncertainty in the exact identification of $k_{z,\text{peak}}$ is caused by the wavenumber resolution, which is tied to the spatial aperture of the $S(r_1, \omega)$.

Further evidence for distinct regimes—low frequency (subsonic) band, a transition band (supersonic at most frequencies), and a high frequency, self-similar (supersonic) band—is shown in Fig. 8 of Ref. 58, where the normalized $|G_0(k_z/k)|$ are plotted for $St = 0.04$ – 4 . For the 10D line array, the transition to supersonic phase speeds occurs around $St = 0.23$, and for the 40D arc around $St = 0.17$. These differences are not due to simply the change in distance, but rather are likely related to either physical differences in the measured sound fields or the need to consider the frequency-dependent nature of the apparent maximum source region. The effects of using a frequency-dependent origin to define θ and thus k_z are explored in Sec. VE.

C. Equivalent acoustic wavepackets

The frequency-dependent axial wavenumber spectra are the Fourier transforms of equivalent acoustic source

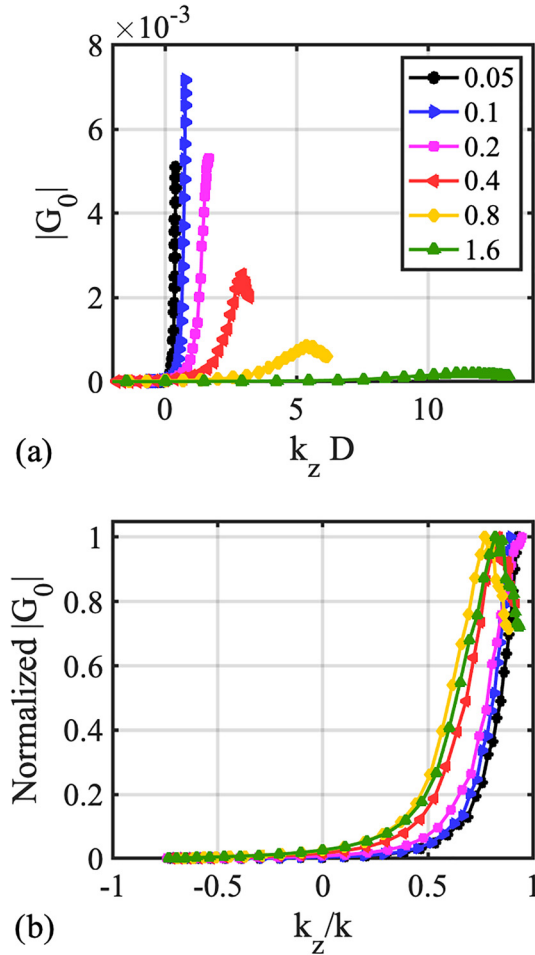


FIG. 7. (Color online) Data-educed, axial wavenumber spectra, $|G_0|$, from the LSS spectral densities (for St in the legend) at the 10D line array as a function of (a) $k_z D$ and (b) k_z/k after normalization.

wavepackets: $G_0(k_z) = \mathcal{F}\{p_w(z)\}$. In this work, the wavepackets are representing the LSS-based contribution to the ESM that produce directional radiation and can be thought of as a surrogate for the azimuthal or optimal mode of the acoustic radiation caused by the complicated turbulent structures.

The LSS-based $|G_0(k_z)|$ are used in an optimization (described in Sec. III B 2) to obtain $p_w(z)$ with the same wavenumber spectra. Examples of the optimized LSS-based wavepackets are shown in Fig. 8 for $St = 0.1, 0.2,$ and 0.4 . The magnitude of the wavepacket is shown as a solid line and the real part is plotted as a dashed line. The oscillations of the real part are related to $k_{z,peak}$ and thus U_c . The wavepackets are plotted as a function of downstream distance relative to the peak (placed at $z = 0$ for these plots) because the exact peak value z_0 cannot be found using the magnitude of the wavenumber spectra. The distances are also scaled by wavelength, λ , to facilitate comparison at different Sr .

The wavepackets obtained from the two input arrays are the same for low St and different for higher Sr . At $St = 0.1$, the wavepacket obtained from the 10D line array (blue) and 40D arc (red) are essentially the same. For higher St , however, the wavepackets from the 40D arc have longer decays than those from the 10D line array. This difference is likely

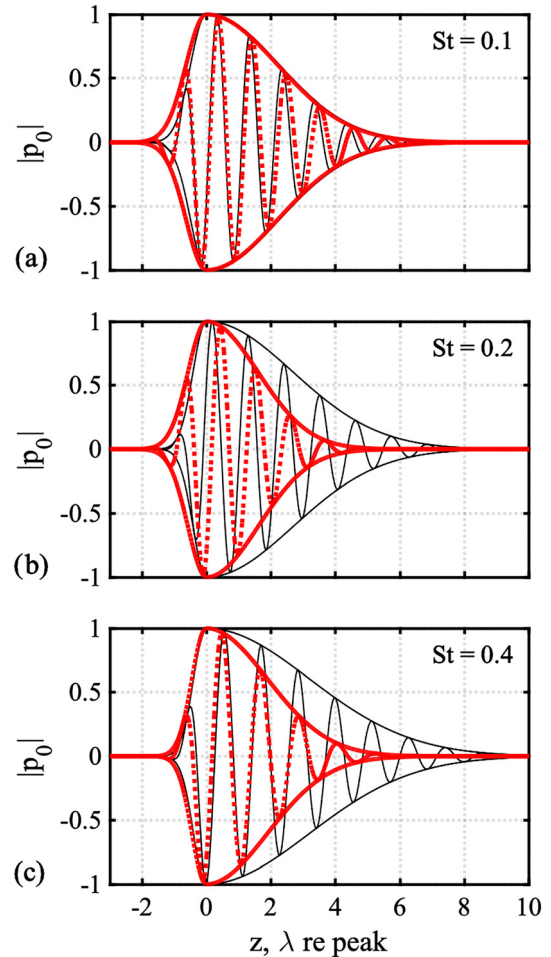


FIG. 8. (Color online) Optimized wavepacket shapes. Magnitude and real part of $p_w(z)$ at (a) $St = 0.1$, (b) $St = 0.2$, and (c) $St = 0.4$ for the 10D line array (thinner black lines) and the 40D arc (thicker red lines), as a function of relative downstream distance, with the peak of each at $z = 0$.

due to the need to account for the frequency-dependent change in maximum apparent source location, which is further discussed in Sec. V E. When the frequency-dependent MARP is used, the wavepackets obtained from the 10D line array and 40D arc have approximately the same shape for $St = 0.2$ and 0.4 . These optimized wavepackets represent an ESM on a cylinder concentric with the jet nozzle.

D. Sound level modeling

The ability of the ESM obtained from the spectral decomposition at one location (r_1) to model sound levels at another location (r_2)—both closer to and farther from the jet—is now evaluated (see Sec. III C for details).

The wavepacket-based levels, L_w , are designed to capture the strong directional radiation assigned to the large-scale similarity spectrum. Examples of L_w for $St = 0.04$ – 2 as a function of scaled downstream distance, z , are shown in Fig. 9(a) for the 10D line array case and Fig. 11(a) for the 40D arc using their respective $|G_0(k_z)|$. The LSS-based L_w matches L_{meas} in the maximum radiation region [shown in Figs. 10(a) and 12(a)]. This agreement is of particular interest for the 10D line array because the similarity spectra (upon which this modeling technique relies) were obtained

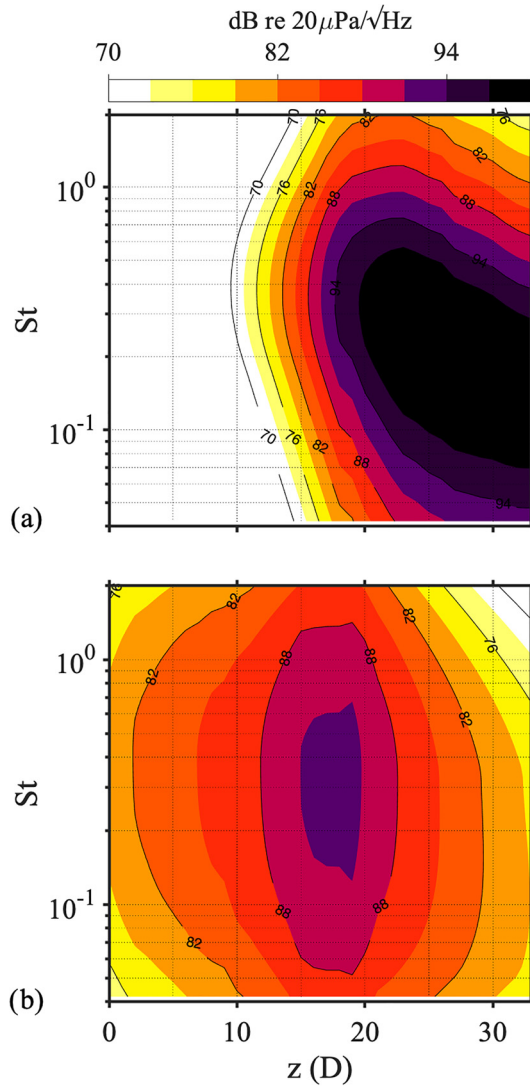


FIG. 9. (Color online) Modeled power spectral density levels on the 10D line array using wavenumber spectra from the same location: (a) L_w and (b) L_i .

from far-field spectra but appears to capture the directional radiation close to the jet as well. At both measurement locations, levels outside the maximum radiation region are underestimated.

To improve the ESM, frequency-dependent FSS-based source distributions are added, as described in Sec. III D. The spatial variation in the portion of the sound ascribed to the FSS spectrum is used to model the fine-scale turbulent mixing noise contribution to the sound field, L_i . Examples of L_i are shown in Fig. 9(b) for the 10D line array and in Fig. 11(b) for the 40D arc. The total modeled field, L_{tot} in Eq. (7), captures the spatial variation in levels better than the L_w alone.

As a benchmark, the differences between L_{tot} and L_{meas} using the same input and modeling locations are calculated. At most angles and frequencies, $|L_{tot} - L_{meas}| < 1$ dB, displayed as white in Figs. 10(b) and 12(b). For the 10D array [Fig. 10(b)], $|L_{tot} - L_{meas}| > 1$ dB occurs at $St > 1.6$ (due to scattering across the linear array of microphones) and near $z = 0$ (due to reflections). These error plots show the consistency of the method. The discrepancies are due to the idealization of the measured spatio-spectral variation as it was

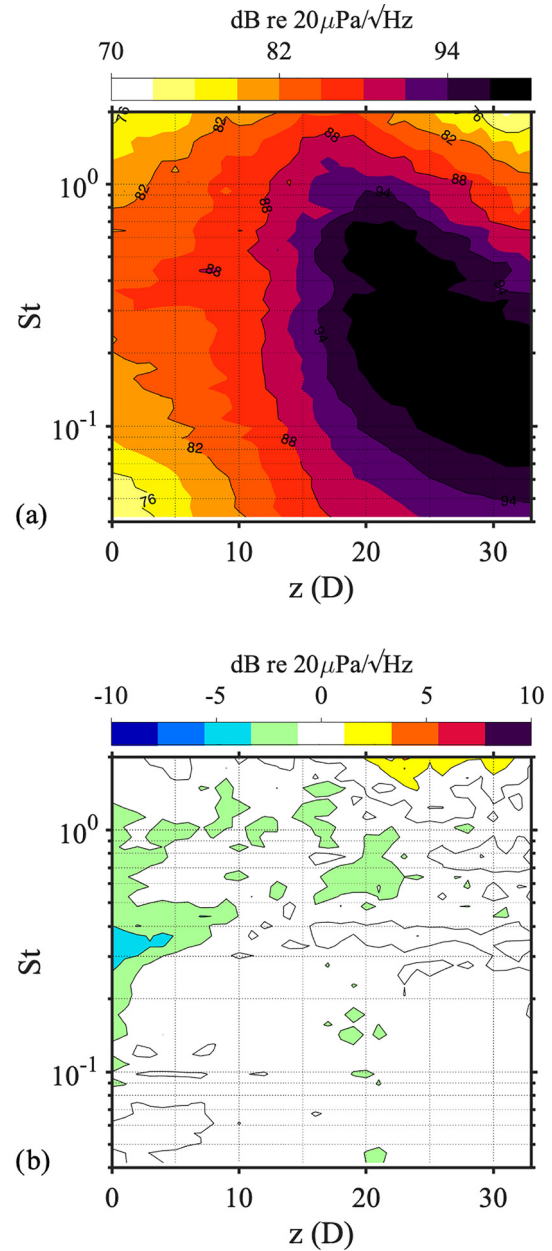


FIG. 10. (Color online) (a) Measured power spectral density levels, L_{meas} , for the 10 D line array and (b) $L_{tot} - L_{meas}$.

decomposed into the LSS and FSS similarity spectra, i.e., the jagged features in the L_{meas} in Figs. 10(a) and 12(a) are smoothed out in L_{tot} .

While the low errors in Figs. 10(b) and 12(b) provide confidence in this modeling technique, the true test comes when the $|G_0(k_z)|$ obtained at one location are used to model levels at a different location. The wavenumber spectra educed from the 40D arc are now used to model the levels on the 10D line array and vice versa. [Extrapolation of $|G_0(k_z)|$ is required because the two measurement apertures span a different set of angles, θ .] The resulting L_{tot} are displayed in Figs. 13(a) and 14(a). For the inward propagation case [Fig. 13(a)], extrapolation effects cause the results for $z < 10D$ to be unphysical, illustrating the difficulty of modeling regions of the sound field that are not sampled by the input array. The errors $|L_{tot} - L_{meas}|$ are shown in Fig. 13(b), using L_{meas} shown in Fig. 10(a). For $z > 12D$, the

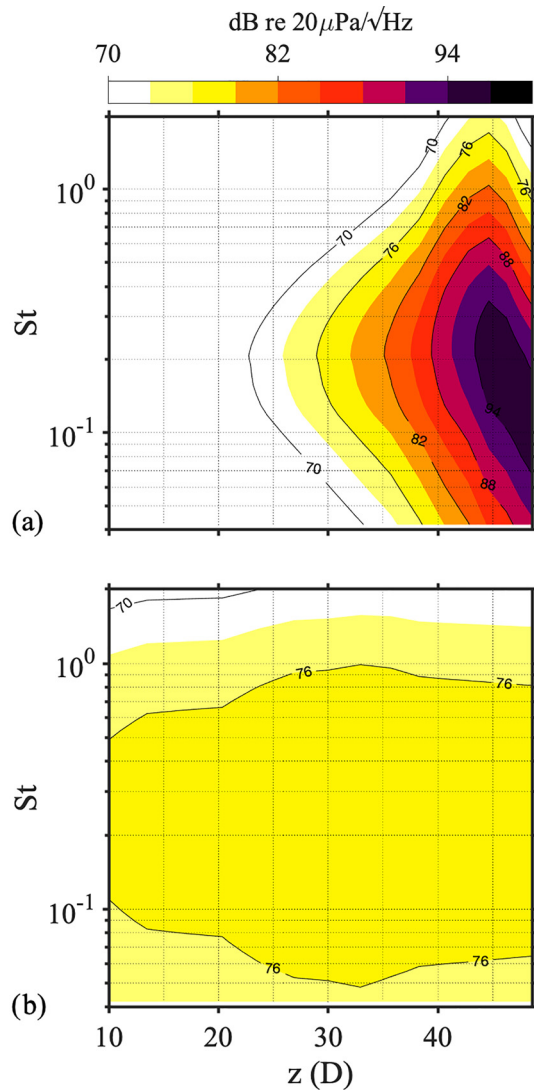


FIG. 11. (Color online) Modeled power spectral density levels on the 40D arc using wavenumber spectra from the same location: (a) L_w and (b) L_i .

prediction is reasonable as the average error magnitude is $|L_{\text{tot}} - L_{\text{meas}}| < 2$ dB for $St < 0.25$. For higher St , however, the error is greater. For the outward propagation case, the difference between L_{tot} [Fig. 14(a)] and L_{meas} [Fig. 12(a)] are shown in Fig. 14(b). The downstream extrapolation of wavenumber spectra ($z > 34D$) works better than the upstream extrapolation, possibly due to the difference in the field correlation in the two regions or the relatively smaller angular range. Additionally, $|L_{\text{tot}} - L_{\text{meas}}| < 2$ dB for $St < 0.25$ and increases at higher St , but in the opposite directions as the inward propagation case.

One possible cause for the errors at higher St relates to the frequency-dependent nature of the extended jet noise source. Many have noted the shift in apparent acoustic source location as frequency increases. For example, a phased-array study by Lee and Bridges¹² for an unheated, subsonic laboratory-scale jet found that the peak source location moved from $z \sim 10D$ at $St = 0.2$ to $z \sim 3D$ at $St = 2$; this shift was confirmed via beamforming by Papamoschou *et al.*⁵⁹ Similar shifts in maximum apparent source location have been found for high-performance military aircraft noise from both uninstalled⁵ and

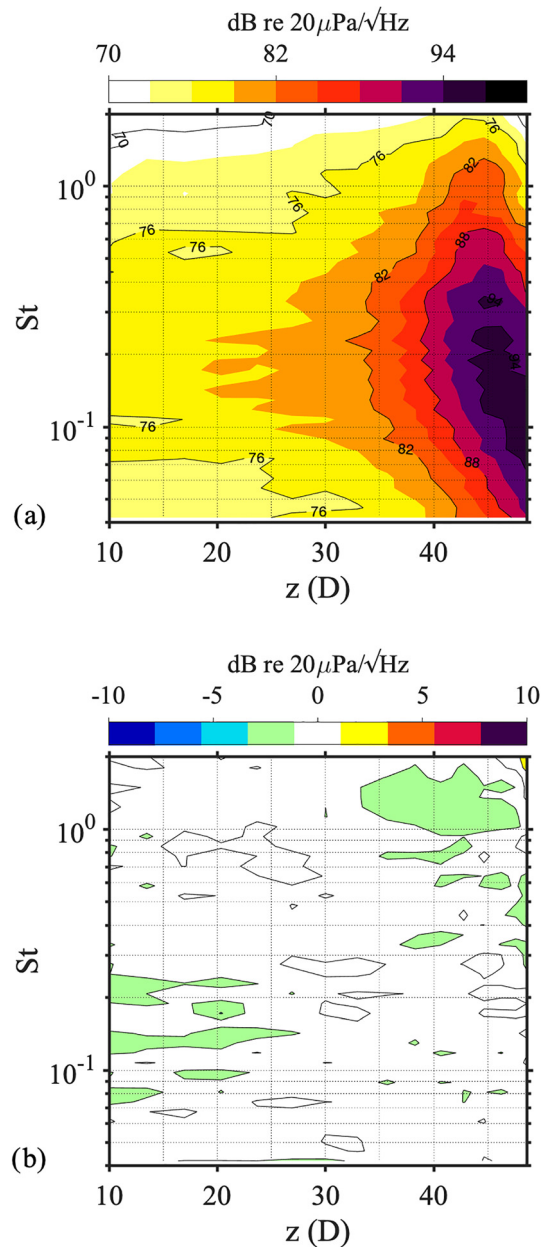


FIG. 12. (Color online) (a) Measured power spectral density levels, L_{meas} , for the 40D arc and (b) $L_{\text{tot}} - L_{\text{meas}}$.

installed engines.^{10,11,16,60,67} The frequency-dependent shift in apparent maximum source location does not translate into significant changes in angle far from the jet. Close to the jet, however, the assumption of a frequency-independent MARP is troublesome as changes in the apparent maximum source region greatly influences the appropriate definition of θ .

E. Frequency-dependent origin

The acoustic vector intensity measured near this Mach 1.8 jet⁵⁷ yields estimates the apparent source location as a function of frequency. The dominant source region—obtained when intensity vectors within 3 dB of the maximum were traced back to the jet centerline—covered $9D < z < 15D$ for $St = 0.1$, $8D < z < 13D$ for $St = 0.2$, $5D < z < 8D$ for $St = 0.4$, and $2D < z < 4D$ for $St = 0.8$, consistent with the idea

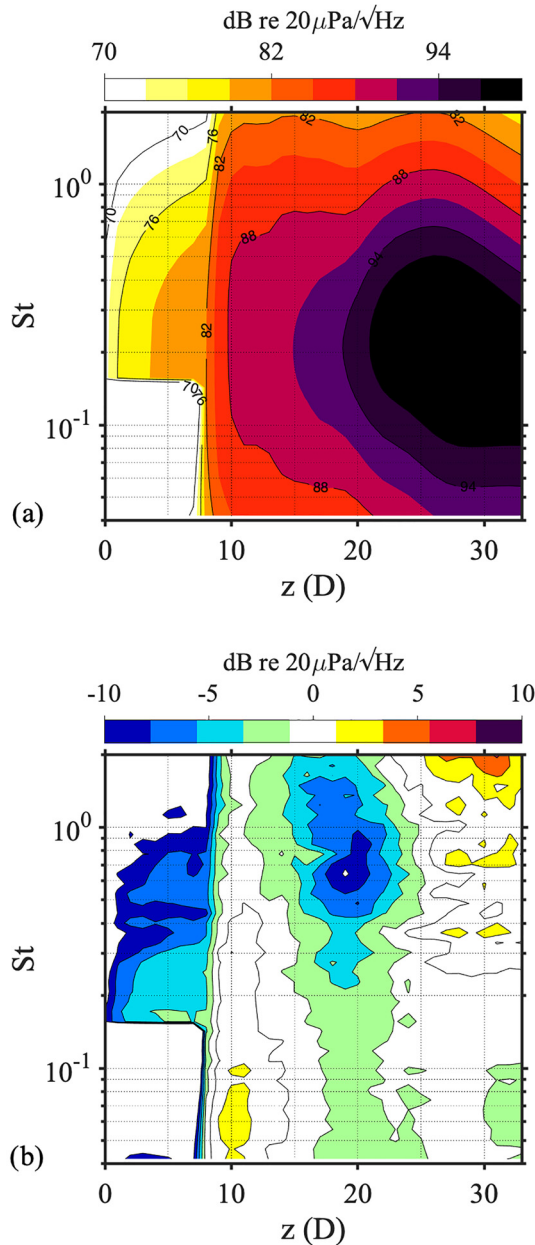


FIG. 13. (Color online) (a) L_{tot} on the 10D line array using wavenumber spectra from the 40D arc, and (b) $L_{\text{tot}} - L_{\text{meas}}$ assuming a constant MARP.

that the source of large-scale turbulent mixing noise contracts and moves upstream as frequency increases. The shift in the location of the dominant source region is further validated by the correlation analyses in Ref. 61.

These intensity results provide a preliminary frequency-dependent MARP for defining θ and, thus, k_z . The MARP remains at $z = 10D$ for $St < 0.25$. For $St > 0.25$, the MARP decreases as St increases as shown in Fig. 15, following the trends identified in Ref. 57. The frequency-dependent MARP is used to generate a new set of LSS-based wavenumber spectra. However, the frequency-independent MARP of $z = 10D$ is still used for the FSS-based incoherent distribution's definition. With the frequency-dependent MARP, the peaks in the LSS-based wavenumber spectra deduced from the 10D line array and the 40D arc are much

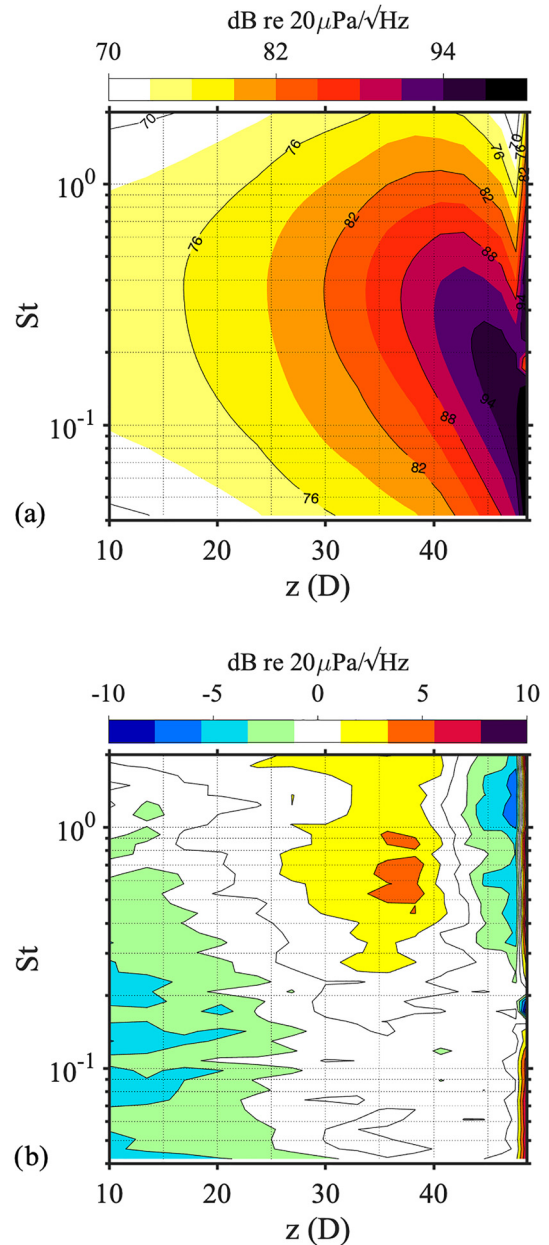


FIG. 14. (Color online) (a) L_{tot} predicted on the 40D arc using wavenumber spectra from the 10D line array, and (b) $L_{\text{tot}} - L_{\text{meas}}$ assuming a constant MARP.

closer to the same value, and the LSS-based wavepackets for $St = 0.2$ and 0.4 are similar at both locations.

This frequency-dependent origin for defining angles improves the sound field modeling for $St > 0.25$. The subsequent predicted L_{tot} using the $|G_0(k_z)|$ at one location to predict the levels at the other location are shown in Figs. 16(a) and 17(a) and match the L_{meas} at higher St better than the constant-MARP predictions. The levels at the 40D arc [errors in Fig. 17(b)] are better modeled than those at the 10D line array [errors in Fig. 16(b)]: Not only are errors lower at high St , but the levels are better reconstructed in the extrapolated region (i.e., the arc locations with angles not spanned by the 10D line array). The better performance of the outward propagation has two implications: (1) close measurements are needed for modeling a large aperture; and

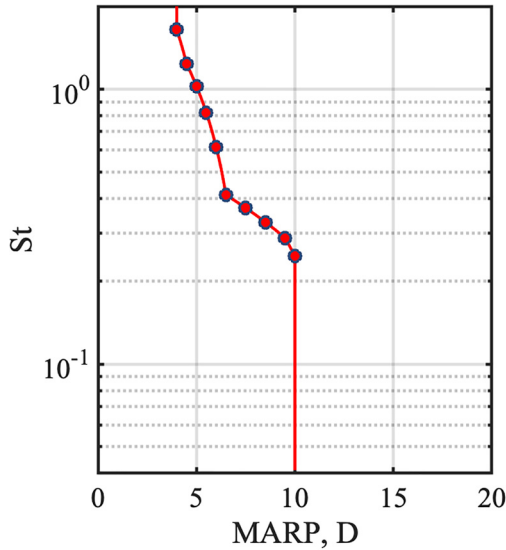


FIG. 15. (Color online) Frequency-dependent MARP used to define θ in obtaining LSS-based wavenumber spectra, $|G_0(k_z)|$.

(2) extrapolation in the downstream direction, where the large-scale turbulent mixing noise dominates, is easier than extrapolating in the sideline or forward direction.

This sound level modeling technique works best when a frequency-dependent MARP is used for the LSS-based wavepackets and the FSS-based distribution uses a constant MARP of $10D$ across all frequencies. The frequency-independent origin for the FSS-based distribution implies a possible maximum apparent region for fine-scale mixing noise that is farther downstream than the peak region of the large-scale mixing noise at high frequencies, which agrees with a ray-tracing source estimation method based on measured acoustic intensity for this Mach 1.8 jet shown in Fig. 6 of Ref. 57. Although this idea may seem counterintuitive, additional support comes from Fig. 1 of Ref. 4 and Figs. 32 and 33 of Ref. 22 showing axial source strength distributions of an unheated, Mach 1.9 jet, where the apparent acoustic source region peak is farther downstream for sideline (fine-scale) radiation than for noise in the peak radiation direction.

F. Convective velocity estimates

Direct measurements of the statistical properties of the velocity fluctuations in jet turbulence have shown that jet centerline velocity, U_j , remains relatively constant during the potential core and then decreases.^{62–68} In addition, U_c/U_j tends to be 0.6–0.8 (cf. Fig. 16 in Ref. 62 and Fig. 21 in Ref. 66). Higher frequencies tend to have higher associated convective speeds because their apparent source region is closer to the end of the potential core than for lower frequencies.^{10–12,26,57,60,69,70} The $|G_0(k_z)|$ provides estimates of $U_c = \omega/k_{z,\text{peak}}$ as the frequency-dependent phase speeds of the frequency-dependent, axial wavepackets, which are related to the directivity, θ_{peak} .

The phase speed ratio U_c/U_j from the LSS-based wavepacket model can be compared to previously reported values (see Sec. III B 3 for details.) For this unheated, Mach 1.8 jet with $\text{Re} = 1.5 \times 10^6$, the average exit centerline velocity

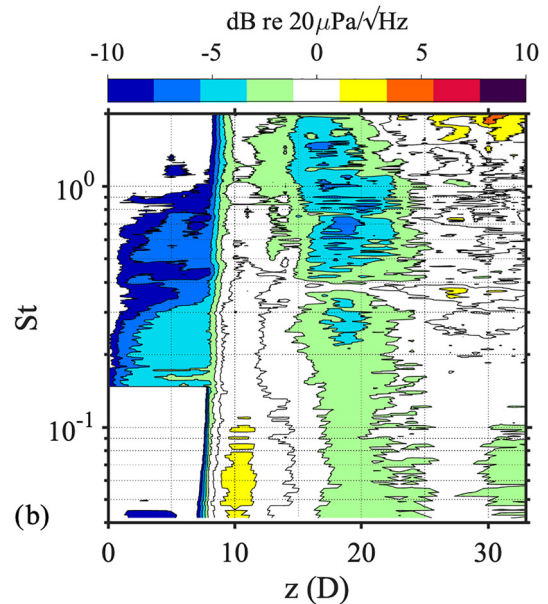
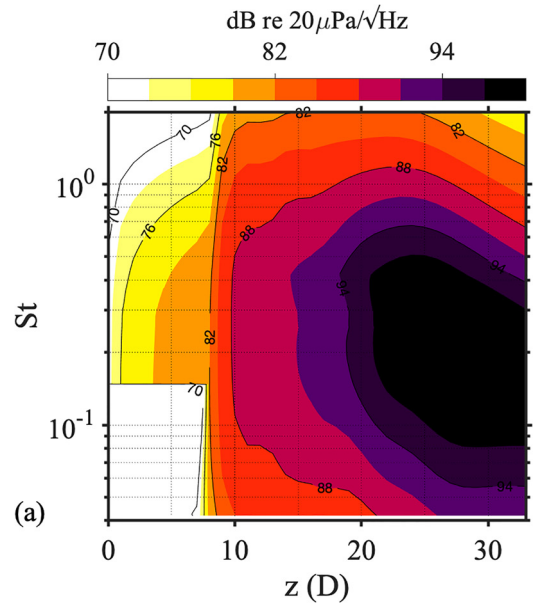


FIG. 16. (Color online) (a) L_{tot} on the $10D$ line array using wavenumber spectra from the $40D$ arc, and (b) $L_{\text{tot}} - L_{\text{meas}}$ using a frequency-dependent MARP.

was $U_j = 488 \text{ m/s}$.² The estimated ratios, shown in Fig. 18(a), range from $U_c/U_j = 0.78\text{--}0.82$ for the $40D$ case and $U_c/U_j = 0.8\text{--}0.88$ for the $10D$ case. These values are larger than the ratios obtained using this method by Morris²⁴ of $U_c/U_j = 0.59$ for $\text{St} = 0.1$ and $U_c/U_j = 0.68$ for $\text{St} = 0.4$, and those found by the Pappaschou²⁶ optimization for analytical wavepacket shapes of $U_c/U_j = 0.44$ for $\text{St} = 0.2$, 0.5 for $\text{St} = 0.5$, and $U_c/U_j = 0.52$ for $\text{St} = 1.0$ for a Mach 0.9 jet. The current estimates from Fig. 18(a) are closer to those found by Du and Morris⁴⁷ using a proper orthogonal decomposition of a large-eddy simulation, where convectively supersonic modes had $U_c/U_j = 0.7$ and 0.8 for $\text{St} = 0.3$ and 0.6 , respectively. A possible cause for the discrepancies between these studies is the radial dependence of the propagation speed of turbulent structures, which can be assessed with two-point correlation

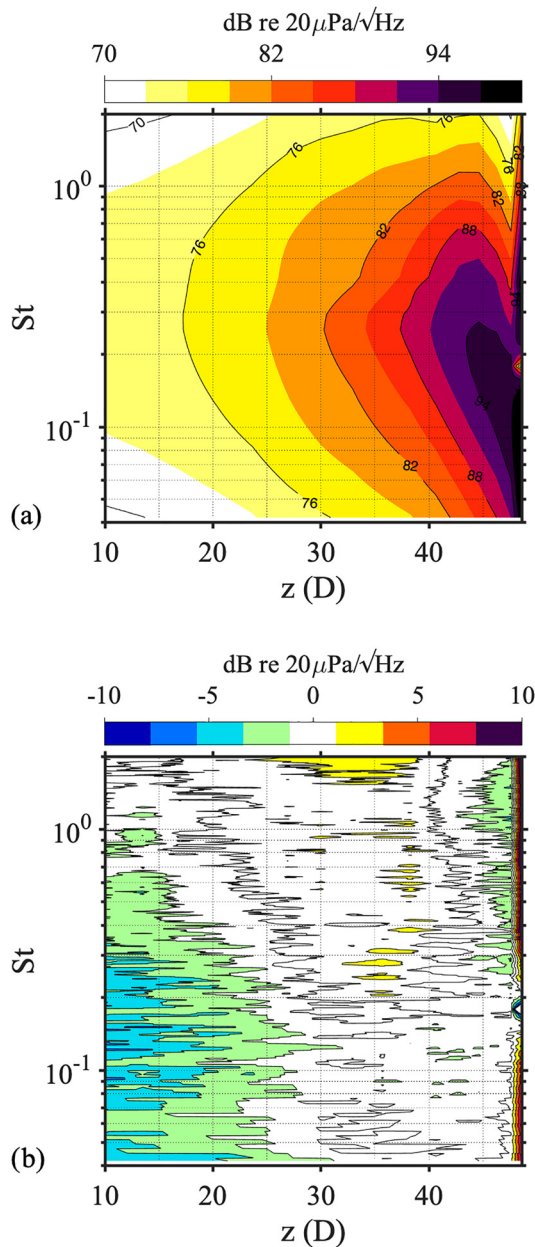


FIG. 17. (Color online) (a) L_{tot} on the 40D arc using wavenumber spectra from the 10D line array, and (b) $L_{\text{tot}} - L_{\text{meas}}$ using a frequency-dependent MARP.

measurements.⁶³ The U_c/U_j estimates from the current wavepacket eduction method for the 40D case appear at the upper accepted ratio of $U_c/U_j = 0.8$, while the results from the 10D case exceed this limit.

One point in favor of these U_c estimates is that the accuracy of the $|G_0(k_z)|$ is more certain for the larger k_z , which correspond to the spatial region where all the noise is assigned to the LSS spectrum [see parts (a) of Figs. 4–6]; whereas smaller k_z are influenced by the inherent uncertainty in assigning portions of the measured spectrum into LSS and FSS spectra.

The estimates of U_c are, however, limited as the resolution and the range of k_z is determined by $k \cos \theta$ of the measurements. No interpolation was used in this analysis; hence, the discrete jumps in the U_c estimates. To evaluate the significance

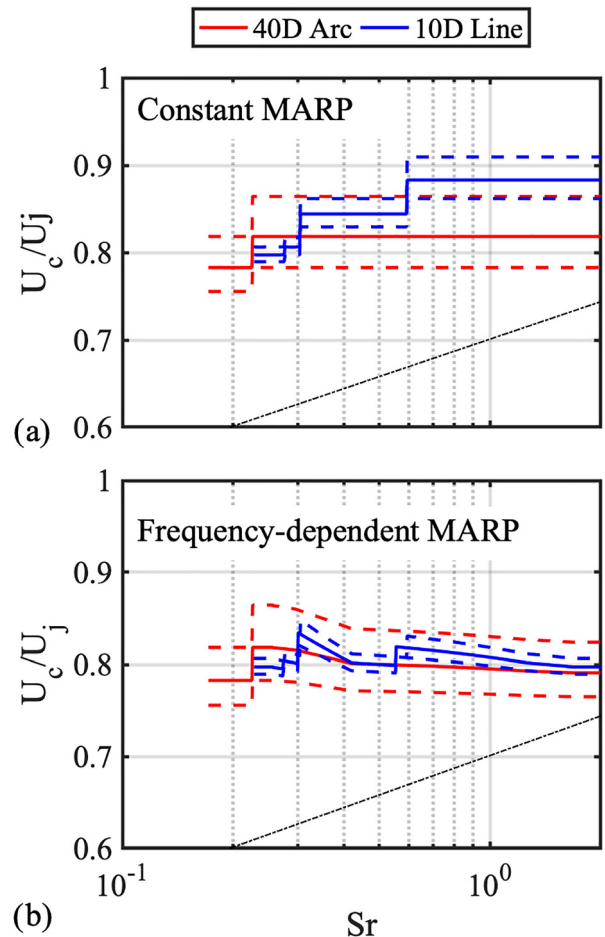


FIG. 18. (Color online) Ratio of convective velocity, U_c , to jet velocity, U_j , from the educed wavepackets using (a) the constant MARP and (b) the frequency-dependent MARP. For all lines, $U_c = \omega/\kappa$. Solid lines use $\kappa = k_{z,\text{peak}}$ (which occurs at the maximum of $|G_0(k_z)|$). Dashed lines have κ as the lower and upper values of k_z for which $|G_0(k_z)| \geq 0.95|G_0(k_{z,\text{peak}})|$ to provide estimate of uncertainty.

of the uncertainty caused by discrete k_z values, the U_c estimates corresponding to a additional k_z values are calculated. The solid lines in Fig. 18(a) show the U_c/U_j obtained using $k_{z,\text{peak}}$ of the $|G_0(k_z)|$ for the constant MARP results. The dashed lines correspond to the ratios for minimum and maximum values of k_z over which $|G_0(k_z)| > 0.95|G_0(k_{z,\text{peak}})|$ are then used to estimate upper and lower bounds on U_c/U_j . These results—shown as dashed lines in Fig. 18(a)—indicate an uncertainty of approximately 10 m/s for the 10D line array estimates and approximately 20 m/s for the 40D arc estimates.

The U_c estimates in Fig. 18(a) correspond to directivity estimates of $\theta_{\text{peak}} = 26^\circ - 36^\circ$ from the 10D line array and $\theta_{\text{peak}} = 24^\circ - 30^\circ$ from the 40D arc. These directivities can be compared to the measured PSD (shown in Fig. 2 of Ref. 57 as a function of θ). The peak levels on the 40D arc occur at 30° for 3.5–10 kHz ($St \approx 0.15 - 0.42$). At higher frequencies, the peak level occurs at 35° , but the levels at 30° and 40° are within 0.5–2 dB up to 50 kHz ($St \approx 2.1$). The relative constancy of the directivity above $St \approx 0.4$ is similar to the θ_{peak} obtained from the 40D arc, but at 30° instead of 35° . The relative constancy across frequency also agrees with the sound intensity direction measured near this jet. As

shown in Fig. 6 of Ref. 57, the maximum intensity vectors' direction is 25° – 35° for frequencies from 2 to 20 kHz.

Because the origin used to define θ impacts the values of k_z , the estimates of θ_{peak} and U_c change when a frequency-dependent MARP is used. While the frequency-dependent MARP in Fig. 15 still needs to be refined, it reduces the frequency variation in estimates of θ_{peak} and U_c , as shown in Fig. 18(b). The U_c/U_j estimates from both the 10D line array and the 40D arc stay close to 0.8, corresponding to fairly constant directivities above $St = 0.3$ for $\theta_{\text{peak}} = 25^\circ$ – 30° . The more realistic ratios for U_c/U_j and θ_{peak} support the idea of using a frequency-dependent MARP to obtain comparable near and far-field results.

VI. CONCLUSIONS

Spectral densities from an unheated Mach 1.8 jet have been employed to obtain a level-based, broadband ESM composed of wavepackets for the large-scale turbulent mixing noise and incoherent, extended source distributions representing fine-scale turbulent mixing noise. The process begins with a similarity spectra decomposition on both the 40D arc and a line array 10D from and parallel to the jet centerline—the closest distance at which this decomposition has been performed. The portion of the spectra assigned to the large-scale mixing noise is used to obtain frequency-dependent, data-educed axial wavenumber spectra, each associated with an equivalent acoustic wavepacket, which can model the directional portion of the sound field associated with the turbulent mixing noise.

Because the wavepacket-modeled sound field does not account for the sound levels outside the maximum radiation region, an incoherent source distribution is created from the portion of the noise assigned to the fine-scale mixing noise. This two-part ESM is employed to model the sound field levels. At the location used to obtain the ESM, the average error in modeled sound levels is less than 2 dB for Strouhal numbers $St = 0.04$ – 1.8 at the 10D line array and $St = 0.04$ – 3.5 at the 40D arc. When modeling the field at the other location, the model's average error is less than 2 dB for $St = 0.04$ – 0.25 but increases for larger St because the apparent directivity changes between the two arrays.

This increase in error with Strouhal numbers likely relates to the extended nature of the source, which complicates the definition of angles close to the jet. A frequency-independent definition of angles is suitable far from the jet, but the frequency-dependent source extent and location need to be accounted for when the data-educed wavenumber spectra are obtained from (or used to model) levels close to the jet. A preliminary attempt at obtaining LSS-based wavepackets using a frequency-dependent definition of angles has shown promise. Better results are obtained, however, when the FSS-based incoherent distribution's angle definition is referenced to a downstream distance of 10D across all frequencies—pointing to a possible maximum apparent region for FSS that is farther downstream than the LSS peak region at high frequencies, similar to Refs. 4, 22, 57, and 60. Estimates of U_c/U_j obtained from the LSS-based wavepackets are approximately 0.8 with the frequency-dependent MARP.

This level-based approach to obtaining an ESM for the turbulent mixing noise from jets has both strengths and limitations compared to more complex approaches. This method can be applied to any set of level-based measurements for which the similarity spectra decomposition is straightforward—meaning it will likely function best in anechoic or ground-based measurements. The input array needs to span a wide range of angles to capture both the LSS and FSS spectral components. This technique is optimal when the angular aperture covered by the input measurements matches that of the desired region of modeling sound levels. The main limitation of this model is that it only obtains sound levels, not other field properties, such as coherence. To obtain estimates of coherence, a multiple-wavepacket ESM is needed, such as those shown in Refs. 16 and 41. Future work may include comparisons with other source characterization methods and sound-level modeling techniques, as well as application to noise from a high-performance military aircraft.

ACKNOWLEDGMENTS

We gratefully acknowledge that support for this research was partially funded by the Office of Naval Research Grant No. N000141410494 for developing wavepacket-based models for jet noise from tactical aircraft. We especially thank the Japan Society for the Promotion of Science for the Invitation Research Fellowship that allowed for these measurements to be obtained. We also thank the reviewers for their helpful comments.

- ¹M. Akamine, Y. Nakanishi, K. Okamoto, S. Teramoto, T. Okunuki, and S. Tsutsumi, "Acoustic phenomena from correctly expanded supersonic jet impinging on inclined plate," *AIAA J.* **53**, 2061–2067 (2015).
- ²M. Akamine, K. Okamoto, K. L. Gee, T. B. Neilsen, S. Teramoto, T. Okunuki, and S. Tsutsumi, "Effect of nozzle-plate distance on acoustic phenomena from supersonic impinging jet," *AIAA J.* **54**, 1943–1952 (2018).
- ³M. Ochmann, "The source simulation technique for acoustic radiation problems," *Acustica* **81**, 512–527 (1995), available at <https://www.ingentaconnect.com/content/dav/aaia/1995/00000081/00000006/art00005>.
- ⁴C. K. W. Tam, N. N. Pasouchenko, and R. H. Schlinker, "Noise source distribution in supersonic jets," *J. Sound Vib.* **291**, 192–201 (2006).
- ⁵R. H. Schlinker, S. A. Liljeborg, D. R. Polak, K. A. Post, C. T. Chipman, and A. M. Stern, "Supersonic jet noise source characteristics and propagation: Engine and model scale," AIAA Paper 2007-3623 (2007).
- ⁶M. J. Lighthill, "On Sound generated aerodynamically. Part 1. General Theory," *Proc. R. Soc. London* **211**, 564–587 (1952).
- ⁷D. K. McLaughlin, C. W. Kuo, and D. Papamoschou, "Experiments on the effect of ground reflections on supersonic jet noise," AIAA Paper 2008-22 (2008).
- ⁸N. P. Valdivia and E. G. Williams, "Study of the comparison of the methods of equivalent sources and boundary element methods for near-field acoustic holography," *J. Acoust. Soc. Am.* **120**, 3694–3705 (2006).
- ⁹J. Hald, "Basic theory and properties of statistically optimized near-field acoustical holography," *J. Acoust. Soc. Am.* **125**, 2105–2120 (2009).
- ¹⁰A. T. Wall, K. L. Gee, T. B. Neilsen, R. L. McKinley, and M. M. James, "Military jet noise source imaging using multisource statistically optimized near-field acoustical holography," *J. Acoust. Soc. Am.* **139**, 1938–1950 (2016).
- ¹¹A. T. Wall, K. L. Gee, K. M. Leete, T. B. Neilsen, T. A. Stout, and M. M. James, "Partial-field decomposition analysis of full-scale supersonic jet noise using optimized-location virtual references," *J. Acoust. Soc. Am.* **144**, 1356–1367 (2018).
- ¹²S. S. Lee and J. Bridges, "Phased-array measurements of single flow hot jets," AIAA Paper 2005-2842 (2005).
- ¹³D. Papamoschou, "Imagining of distributed directional noise sources," *J. Sound Vib.* **330**, 2265–2280 (2011).

- ¹⁴T. Suzuki and T. Colonius, "Instability waves in a subsonic round jet detected using a near-field phased microphone array," *J. Fluid Mech.* **565**, 197–226 (2006).
- ¹⁵T. Suzuki, "Coherent noise sources of a subsonic round jet investigated using hydrodynamics and acoustic phased-array microphones," *J. Fluid Mech.* **730**, 659–698 (2013).
- ¹⁶B. M. Harker, K. L. Gee, T. B. Neilsen, A. T. Wall, and M. M. James, "Beamforming-based wavepacket model for noise environment predictions of tactical aircraft," AIAA Paper 2017-4048 (2017).
- ¹⁷J. Morgan, T. B. Neilsen, K. L. Gee, A. T. Wall, and M. M. James, "Simple-source model of high-power jet aircraft noise," *Noise Control Eng. J.* **60**, 435–449 (2012).
- ¹⁸C. K. W. Tam, M. Golebiowski, and J. M. Seiner, "On the two components of turbulent mixing noise from supersonic jets," AIAA Paper 96-1716 (1996).
- ¹⁹C. K. W. Tam and K. B. M. Q. Zaman, "Subsonic jet noise from nonaxisymmetric and tabbed nozzles," *AIAA J.* **38**, 592–599 (2000).
- ²⁰R. H. Schlinker, "Supersonic jet noise experiments," Ph.D. thesis, Department of Aerospace Engineering, University of Southern California, Los Angeles, CA, 1975.
- ²¹K. Viswanathan, "Analysis of the two similarity components of turbulent mixing noise," *AIAA J.* **40**, 1735–1744 (2002).
- ²²C. K. W. Tam, K. Viswanathan, K. K. Ahuja, and J. Panda, "The sources of jet noise: Experimental evidence," *J. Fluid Mech.* **615**, 253–292 (2008).
- ²³T. B. Neilsen, K. L. Gee, A. T. Wall, and M. M. James, "Similarity spectra analysis of high-performance jet aircraft noise," *J. Acoust. Soc. Am.* **133**, 2116–2125 (2013).
- ²⁴P. J. Morris, "A note on noise generation by large scale turbulent structures in subsonic and supersonic jets," *Int. J. Aeroacoust.* **8**, 301–315 (2009).
- ²⁵T. B. Neilsen, K. L. Gee, B. M. Harker, and M. M. James, "Level-educed wavepacket representation of noise radiation from a high-performance military aircraft," AIAA Paper 2016-1880 (2016).
- ²⁶D. Papamoschou, "Wavepacket modeling of jet noise sources," AIAA Paper 2011-2835 (2011).
- ²⁷D. Papamoschou, "Prediction of jet noise shielding," AIAA Paper 2010-0653 (2010).
- ²⁸A. Michalke, "On the effect of spatial source coherence on the radiation of jet noise," *J. Sound Vib.* **55**, 377–394 (1977).
- ²⁹D. G. Crighton and P. Huerre, "Shear-layer pressure fluctuations and superdirective acoustic sources," *J. Fluid Mech.* **220**, 355–368 (1990).
- ³⁰P. Jordan and T. Colonius, "Wave packets and turbulent jet noise," *Ann. Rev. Fluid Mech.* **45**, 173–195 (2013).
- ³¹O. T. Schmidt, A. Towne, G. Rigas, T. Colonius, and G. A. Brès, "Spectral analysis of jet turbulence," *J. Fluid Mech.* **855**, 953–982 (2018).
- ³²O. Semeraro, L. Lesshafft, V. Jaunet, and P. Jordan, "Modeling of coherent structures in a turbulent jet as global linear instability wavepackets: Theory and experiment," *Int. J. Heat Fluid Flow* **62**, 24–32 (2016).
- ³³X. Garnaud, L. Lesshafft, P. J. Schmid, and P. Huerre, "The preferred mode of incompressible jets: Linear frequency response analysis," *J. Fluid Mech.* **716**, 189–202 (2013).
- ³⁴A. Towne, T. Colonius, P. Jordan, A. V. G. Cavalieri, and G. A. Brès, "Stochastic and nonlinear forcing of wavepackets in a Mach 0.9 jet," AIAA Paper 2015-2217 (2015).
- ³⁵O. T. Schmidt and P. J. Schmid, "Statistics of stochastics: A conditional space-time POD formalism for intermittent and rare events with application to jet noise," arXiv:1811.07962 (2018).
- ³⁶K. Sasaki, A. V. Cavalieri, P. Jordan, O. T. Schmidt, T. Colonius, and G. A. Brès, "High-frequency wavepackets in turbulent jets," *J. Fluid Mech.* **830**, R2-1–R2-12 (2017).
- ³⁷J. Jeun, J. W. Nichols, and M. R. Jovanović, "Input-output analysis of high-speed axisymmetric isothermal jet noise," *Phys. Fluids* **28**, 047101 (2016).
- ³⁸J. Ffowcs Williams, "The noise from turbulence convected at high speed," *Philos. Trans. R. Soc. A* **255**, 469–503 (1963).
- ³⁹B. M. Harker, T. B. Neilsen, K. L. Gee, A. T. Wall, and M. M. James, "Spatiotemporal correlation analysis of jet noise from a high-performance military aircraft," *AIAA J.* **54**(5), 1554–1566 (2016).
- ⁴⁰C. Bailly and K. Fujii, "High-speed jet noise," *Mech. Eng. Rev.* **13**, 1–13 (2016).
- ⁴¹A. V. G. Cavalieri and A. Agarwal, "Coherence decay and its impact on sound radiation by wavepackets," *J. Fluid Mech.* **748**, 399–415 (2014).
- ⁴²R. Reba, S. Narayanan, and T. Colonius, "Wave-packet models for large-scale mixing noise," *Int. J. Aeroacoust.* **9**, 533–558 (2010).
- ⁴³A. Sinha, D. Rodriguez, G. A. Brès, and T. Colonius, "Wavepacket models for supersonic jet noise," *J. Fluid Mech.* **742**, 71–95 (2014).
- ⁴⁴I. Maia, P. Jordan, V. Jaunet, and A. V. Cavalieri, "Two-point wavepacket modelling of jet noise," AIAA Paper 2017-3380 (2017).
- ⁴⁵W. J. Baars and C. E. Tinney, "Proper orthogonal decomposition-based spectral higher-order stochastic estimation," *Phys. Fluids* **26**, 055112 (2014).
- ⁴⁶M. Koenig, A. V. G. Cavalieri, P. Jordan, J. Delville, Y. Gervais, and D. Papamoschou, "Farfield filtering and source imaging of subsonic jet noise," *J. Sound Vib.* **332**, 4067–4088 (2013).
- ⁴⁷Y. Du and P. J. Morris, "Simulation of the effect of a low by-pass cooling stream on supersonic jet noise," AIAA Paper 2014-1402 (2014).
- ⁴⁸R. H. Schlinker, J. C. Simonich, D. W. Shannon, R. A. Reba, T. Colonius, K. Gudmundsson, and F. Ladeinde, "Supersonic jet noise from round and chevron nozzles: Experimental studies," AIAA Paper No. 2009-3257.
- ⁴⁹R. H. Schlinker, J. C. Simonich, R. A. Reba, T. Colonius, and F. Ladeinde, "Decomposition of high speed jet noise: Source characteristics and propagation effects," AIAA Paper 2008-2890 (2008).
- ⁵⁰K. Viswanathan, "Does a model-scale nozzle emit the same jet noise as a jet engine?," *AIAA J.* **46**, 1715–1737 (2008).
- ⁵¹K. Viswanathan and M. J. Czech, "Role of jet temperature in correlating jet noise," *AIAA J.* **47**, 1090–1106 (2009).
- ⁵²A. B. Vaughn, T. B. Neilsen, K. L. Gee, K. Okamoto, and M. Akamine, "Near-field spatial variation in similarity spectra decomposition of a Mach 1.8 laboratory-scale jet," *Proc. Mtgs. Acoust.* **29**, 045004 (2016).
- ⁵³J. Liu, K. Kailasanath, and E. J. Gutmark, "Similarity spectra analysis of highly heated supersonic jets using large-eddy simulations," AIAA Paper 2017-0926 (2017).
- ⁵⁴T. B. Neilsen, K. L. Gee, A. T. Wall, M. M. James, and A. A. Atchley, "Comparison of supersonic full-scale and laboratory-scale jet data and the similarity spectra for turbulent mixing noise," *Proc. Mtgs. Acoust.* **19**, 040071 (2013).
- ⁵⁵K. M. Leete, A. T. Wall, K. L. Gee, T. B. Neilsen, B. M. Harker, and M. M. James, "Azimuthal coherence of the sound field in the vicinity of a high-performance military aircraft," *Proc. Mtgs. Acoust.* **29**, 045007 (2016).
- ⁵⁶B. Greska, "Supersonic jet noise and its reduction using microjet injection," Ph.D. thesis, The Florida State University, FAMU-FSU Collage of Engineering, Tallahassee, FL, 2005.
- ⁵⁷K. L. Gee, M. Akamine, K. Okamoto, T. B. Neilsen, M. Cook, S. Tsutsumi, S. Teramoto, and T. Okuuki, "Characterization of supersonic laboratory-scale jet noise with vector acoustic intensity," AIAA Paper 2017-3519 (2017).
- ⁵⁸T. B. Neilsen, A. B. Vaughn, K. L. Gee, M. Akamine, K. Okamoto, S. Teramoto, and S. Tsutsumi, "Level-educed wavepacket representation of Mach 1.8 laboratory-scale jet noise," AIAA Paper 2017-4049 (2017).
- ⁵⁹D. Papamoschou, P. J. Morris, and D. K. McLaughlin, "Beamformed flow-acoustic correlations in high-speed jets," AIAA Paper 2009-3212 (2009).
- ⁶⁰T. A. Stout, K. L. Gee, T. B. Neilsen, A. T. Wall, and M. M. James, "Source characterization of full-scale jet noise using acoustic intensity," *Noise Control Eng. J.* **63**, 522–536 (2015).
- ⁶¹J. A. Ward, S. H. Swift, K. L. Gee, T. B. Neilsen, K. Okamoto, and M. Akamine, "Frequency-dependent jet noise source localization using cross-correlation between near and far-field microphone arrays," *Proc. Mtgs. Acoust.* **31**, 040005 (2017).
- ⁶²M. Harper-Bourne, "Jet noise turbulence measurements," AIAA Paper 2003-3214 (2003).
- ⁶³P. J. Morris and K. B. M. Q. Zaman, "Velocity measurements in jets with application to noise source modeling," *J. Sound Vib.* **329**, 394–414 (2010).
- ⁶⁴J. C. Lau, "Effects of exit Mach number and temperature on mean-flow and turbulence characteristics in round jets," *J. Fluid Mech.* **105**, 193–218 (1981).
- ⁶⁵W. J. Baars, C. E. Tinney, N. E. Murray, B. J. Jansen, and P. Panickar, "The effect of heat on turbulent mixing noise in supersonic jets," AIAA Paper 2011-1029 (2011).

- ⁶⁶N. E. Murray and G. W. Lyons, "On the convective velocity of source events related to supersonic jet crackle," *J. Fluid Mech.* **793**, 477–503 (2016).
- ⁶⁷B. Greska and A. Krothapalli, "A near-field study of high temperature supersonic jets," AIAA Paper 2008-3026 (2008).
- ⁶⁸T. R. Troutt and D. K. McLaughlin, "Experiments on the flow and acoustic properties of a moderate-Reynolds-number supersonic jet," *J. Fluid Mech.* **116**, 123–156 (1982).
- ⁶⁹C. E. Tinney, L. S. Ukeiley, and M. N. Glauser, "Low-dimensional characteristics of a transonic jet. Part 1. Proper orthogonal decomposition," *J. Fluid Mech.* **612**, 107–141 (2008).
- ⁷⁰K. M. Leete, A. T. Wall, K. L. Gee, T. B. Neilsen, M. M. James, and J. M. Downing, "Dependence of high-performance military aircraft noise on frequency and engine power," AIAA Paper 2018-2826 (2018).